

# SCP: Spherical-Coordinate-based Learned Point Cloud Compression

Ao Luo<sup>1,2</sup>, Linxin Song<sup>2</sup>, Keisuke Nonaka<sup>1</sup>, Kyohei Unno<sup>1</sup>,  
Heming Sun<sup>2</sup>, Masayuki Goto<sup>2</sup>, Jiro Katto<sup>2</sup>

<sup>1</sup>KDDI Research Inc.

<sup>2</sup>Waseda University

xao-luo, ki-nonaka, ky-unno@kddi.com, songlx.imse.gt@ruri.waseda.jp,  
hemingsun@aoni.waseda.jp, masagoto, katto@waseda.jp

## Abstract

In recent years, the task of learned point cloud compression has gained prominence. An important type of point cloud, the spinning LiDAR point cloud, is generated by spinning LiDAR on vehicles. This process results in numerous circular shapes and azimuthal angle invariance features within the point clouds. However, these two features have been largely overlooked by previous methodologies. In this paper, we introduce a model-agnostic method called Spherical-Coordinate-based learned Point cloud compression (SCP), designed to leverage the aforementioned features fully. Additionally, we propose a multi-level Octree for SCP to mitigate the reconstruction error for distant areas within the Spherical-coordinate-based Octree. SCP exhibits excellent universality, making it applicable to various learned point cloud compression techniques. Experimental results demonstrate that SCP surpasses previous state-of-the-art methods by up to 29.14% in point-to-point PSNR BD-Rate.

## 1 Introduction

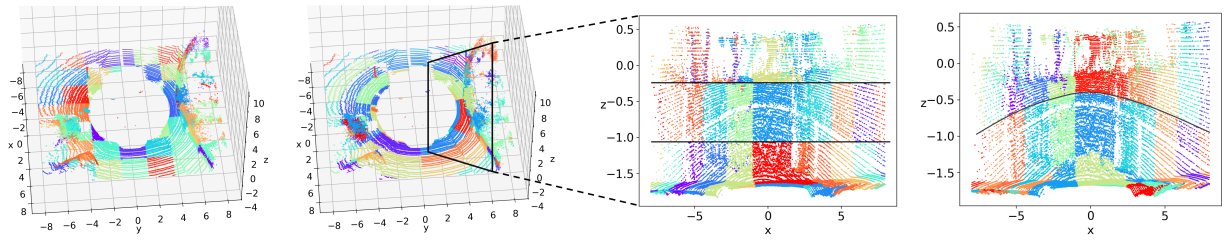
LiDAR point clouds play a crucial role in numerous real-world applications, including self-driving vehicles (Li et al. 2020; Fernandes et al. 2021; Silva et al. 2023), robotics (He et al. 2021b, 2020; Wang et al. 2019) and 3D mapping (Choe et al. 2021; Li et al. 2021). However, the transmission and storage of these point clouds present significant challenges. A typical large point cloud may contain up to a million points (Quach, Valenzise, and Dufaux 2019), making direct storage highly inefficient.

In an effort to mitigate the transmission and storage costs associated with point clouds, MPEG introduced a hand-crafted compression standard known as Geometry-based Point Cloud Compression (G-PCC) (ISO/IEC JTC 1/SC 29/WC 7 2021). This standard employs different geometric structures, including the Octree (Jackins and Tanimoto 1980) and predictive geometry (ISO/IEC JTC 1/SC 29/WC 7 2019), to compress point clouds. The Octree-based entropy model is a widely adopted approach in both G-PCC and learned methods for representing and compressing point clouds. Simultaneously, another geometric structure, predictive geometry, capitalizes on the chain structure formed by each LiDAR laser beam. It predicts the position of the next point based on the angles and distances of preceding points on the chain. Other than basic G-PCC, a Cylindrical-coordinate-based method (Srid-

hara, Pavez, and Ortega 2021) suggests transforming the Cartesian-coordinate positions into Cylindrical coordinates for G-PCC to compress. In the Cylindrical coordinates, when splitting  $\theta$  coordinate for Octree construction, points from the same chain (points acquired by the same laser beam) tend to be grouped into the same voxel, as shown in Fig. 1(b)-left. Thus, these points have more relevant information in their context for compressing. Consequently, this method improves the performance of G-PCC. Concurrently, learned point cloud compression methods are emerging. Techniques such as OctSqueeze (Huang et al. 2020), VoxelDNN (Nguyen et al. 2021a), VoxelContext-Net (Que, Lu, and Xu 2021), and OctFormer (Cui et al. 2023) employ information of ancient voxels for prediction of the current one. Advancing these approaches, OctAttention (Fu et al. 2022), SparsePCGC (Wang et al. 2022), and EHEM (Song et al. 2023) harness the voxels in the same level as the current one to minimize the redundancy.

Nevertheless, the aforementioned learned methods overlook a crucial feature of spinning LiDAR point clouds. Fig. 1(a) visualizes a spinning LiDAR point cloud. This LiDAR generates numerous circular-shaped point chains within the point clouds, leading to high redundancy. The predictive geometry in G-PCC utilizes spherical coordinates for encoding point chains, but it solely uses the information of points within the same chain as references, disregarding other neighboring points. The Cylindrical coordinates (Sridhara, Pavez, and Ortega 2021) inadequately represent point clouds since points in the same chain have different  $z$  coordinates, causing separation in different voxels, as shown in Fig. 1(b)-right. Fortunately, inspired by predictive geometry, we find these points share the same azimuthal angle, leading to the use of Spherical coordinates where the azimuthal angle replaces the  $z$  coordinate. This transformation allows points in the same chain to be split in the same voxel, concentrating the relevant information, as shown in Fig. 1(c).

In this paper, we focus on the spinning LiDAR point cloud, which is called LiDAR PC for abbreviation. To fully leverage the circular-shaped azimuthal-angle-invariant point chains in LiDAR PCs, we introduce a model-agnostic Spherical-Coordinate-based learned Point cloud compression (SCP) method. SCP transforms LiDAR PCs from Cartesian coordinates to Spherical coordinates, concentrating the relevant information and making it easier for neural



(a) The Octree structure produced in Cartesian coordinates. (b) The Octree structure produced in Cylindrical coordinates. (c) The Octree structure produced in Spherical coordinates.

Figure 1: Comparison of the Octree structures in Cartesian, Cylindrical, and Spherical coordinates. The points with the same color are in the same voxel. When looking up-down, the Octree structure in Cylindrical coordinates (see Fig. 1(b)-left) can better fit the LiDAR point clouds than Cartesian coordinates because it harnesses the circular shapes of LiDAR point clouds. In this up-down view, the Octree structures of Cylindrical and Spherical coordinates are similar. However, when looking from the original point horizontally, as the black lines in Fig. 1(b)-right and Fig. 1(c), the Octree in Cylindrical coordinates overlooks the azimuthal angle invariance, often splitting chains into different voxels. In contrast, the Octree in Spherical coordinates tends to group points from the same chain into the same voxel, increasing the relevant information for every point.

networks to reduce redundancy. It’s important to note that, as SCP primarily alters the data pre-processing methods, it is model-agnostic and can be applied to various learned point cloud compression methods. In our experiments, we demonstrate its effectiveness by applying SCP to recent Cartesian-coordinate-based methods like EHEM (Song et al. 2023) and OctAttention (Fu et al. 2022). Additionally, as shown in Fig. 2, the distant voxels in the Spherical-coordinate-based Octree have larger voxel sizes than the central voxels, and the voxel size is positively correlated with the reconstruction errors, resulting in higher reconstruction errors for distant voxels. To solve this problem, we propose a multi-level Octree for SCP, which assigns additional levels to distant voxels. With more levels, the voxel size decreases, leading to lower reconstruction errors.

We trained and evaluated the baseline methods and SCP on the SemanticKITTI (Behley et al. 2019) and Ford (Pandey, McBride, and Eustice 2011) datasets. According to our experiment results, SCP surpasses previous state-of-the-art methods in all conducted experiments. The contributions of our work can be summarized as follows: (1) We introduce a model-agnostic Spherical-Coordinate-based learned Point cloud compression (SCP) method. This method transforms point clouds into Spherical coordinates, thereby fully leveraging the circular shapes and the azimuthal angle invariance feature inherent in LiDAR PCs, (2) we propose a multi-level Octree structure, which mitigates the increment of reconstruction error of distant voxels in the Spherical-coordinate-based Octree, and (3) our experiments, conducted on various backbone methods, demonstrate that our methods can efficiently reduce redundancy among points, surpassing previous state-of-the-art methods by up to 29.14% in point-to-point PSNR BD-Rate (Brulants, Munteanu, and Schelkens 2015).

## 2 Related Work

### 2.1 Hand-Crafted Methods

Hand-crafted methods based on geometry typically employ tree structures like Octree (Jackins and Tanimoto 1980; Gar-

cia and de Queiroz 2018; Unno et al. 2023) and predictive geometry (ISO/IEC JTC 1/SC 29/WC 7 2019) to organize unstructured point clouds. The Octree structure is widely used in numerous methods, such as (Huang et al. 2008; Kammerl et al. 2012). Predictive geometry, on the other hand, models LiDAR PCs as a predictive tree, where each branch represents a complete point chain scanned by a laser beam. This approach leverages the circular chain structure in LiDAR PCs to predict subsequent points based on the angles and distances of previous points in the chain. Leveraging the circular shape of LiDAR PCs, (Sridhara, Pavez, and Ortega 2021) proposed a transformation from Cartesian-coordinate-based positions to Cylindrical coordinates. This approach, being sensitive to circular shapes, enhances the performance of the G-PCC algorithm in compressing point clouds.

### 2.2 Learned Point Cloud Compression Methods

In recent years, learned point cloud compression methods have been emerging. Many of these techniques, including those cited in (Nguyen et al. 2021b; Quach, Valenzise, and Dufaux 2019; Que, Lu, and Xu 2021; Nguyen et al. 2021a; Wang et al. 2022), utilize Octree to represent and compress point clouds.

OctSqueeze (Huang et al. 2020) builds the Octree of the point cloud, predicting voxel occupancy level by level, using information from ancient voxels and known data about the current voxel. Building upon OctSqueeze, methods such as VoxelDNN (Nguyen et al. 2021a), VoxelContext-Net (Que, Lu, and Xu 2021), SparsePCGC (Wang et al. 2022), and OctFormer (Cui et al. 2023) eliminate redundancy by employing the information of neighbor voxels of the parent voxel. Moreover, Surface Prior (Chen et al. 2022) incorporates neighbor voxels which share the same depth as the current coding voxel, into the framework. OctAttention (Fu et al. 2022) further utilizes this kind of voxel, increasing the context size from surrounding 26 voxels to 1024 voxels. This significantly expands the receptive field of the current voxel. Building on OctAttention, EHEM (Song et al. 2023) further exploits the potential of the Transformer framework by in-

tegrating the Swin Transformer (Liu et al. 2021) into their method. This effectively increases the context size to 8192 sibling voxels. Simultaneously, it transitions from serial coding to a checkerboard (He et al. 2021a) type, resulting in a substantial reduction in decoding time. In another aspect, (Chen et al. 2022) employs a context with uncle voxels and utilizes the feature of circular shapes in the LiDAR PCs by incorporating a geometry-prior loss for training.

### 3 Preliminary

In this section, we explain the Octree structure, which efficiently represents the point clouds. Then the coordinate systems involved in our proposed method are introduced. Finally, our optimizing target is illustrated.

#### 3.1 Octree Structure

The Octree is a hierarchical data structure that provides an efficient way of representing 3D point clouds and is beneficial for dealing with inherently unstructured and sparse LiDAR PCs. When constructing the Octree, the whole point cloud is taken as a cube, a.k.a a voxel, then divided into 8 equal-sized sub-voxels. This procedure repeats until the side length of a leaf voxel is equal to the quantization step. Then the quantization operation merges points in the same leaf voxel together. In each non-leaf voxel, the sub-voxels with points in them are represented by a bit 1, and the empty ones are set to value 0. Therefore, each non-leaf voxel is represented by an occupancy symbol composed of 8 bits ( $1 - 255$ ), where each bit indicates the occupancy status of the corresponding sub-voxel.

#### 3.2 Coordinate Systems

We introduce different coordinate systems involved in our experiments: 3-D Cartesian coordinates, Cylindrical coordinates, and Spherical coordinates.

**3-D Cartesian Coordinate System** describes each point in the space by 3 numerical coordinates, which are the signed distances from the point to three mutually perpendicular planes. These coordinates are given as  $(x, y, z)$ .

**Cylindrical Coordinate System** is a natural extension of polar coordinates. It describes a point by three values: radial distance  $\rho$  from the origin, the angular coordinate  $\theta$  (the same as in polar coordinates), and the height  $z$ , which is the same as in Cartesian coordinates. The transformation from Cartesian coordinates to Cylindrical coordinates can be written as:

$$\rho = \sqrt{x^2 + y^2}, \theta = \arctan \frac{y}{x}, z = z, \quad (1)$$

note that the quadrant of  $\theta$  is decided by signs of  $x$  and  $y$ .

**Spherical Coordinate System** also describes a point with three values: the radial distance  $\rho$  from the origin to the point, and two angles: the polar angle  $\theta$ , which is the same angle used in cylindrical coordinates, and the azimuthal angle  $\varphi$ , which is the angle from the positive  $z$  coordinate to the point. The transformation equations from Cartesian coordinates are:

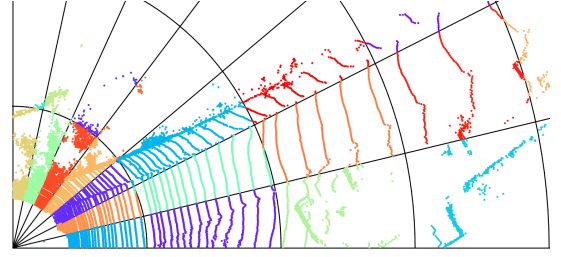


Figure 2: In Spherical coordinates, the size of the voxels varies based on their distance from the origin (left-bottom corner). We distinguish voxels by different colors. The sizes of distant voxels are larger than those of the central ones. This phenomenon results in lower reconstruction errors for the central voxels and higher errors for the distant ones.

$$\rho = \sqrt{x^2 + y^2 + z^2}, \theta = \arctan \frac{y}{x}, \varphi = \arccos \frac{z}{\rho}, \quad (2)$$

again, the quadrant of  $\theta$  depends on the signs of  $x$  and  $y$ .

#### 3.3 Task Definition

The occupancy sequence  $\mathbf{x} = \{x_1, \dots, x_V\}$  ( $V$  is the number of voxels) of voxels in an Octree is losslessly encoded by an entropy encoder into a bitstream, based on the predicted probability from a neural network. After transmission, the Octree is reconstructed from the entropy-decoded occupancy sequence and converted back into the point cloud. Hence, the objective of point cloud geometry compression is to predict the occupancy of each voxel in the Octree, which can be viewed as a 255-category classification problem. Given all the parameters in our model as  $\mathbf{w}$  and context information as  $\mathbf{C} = \{\mathbf{C}_1, \dots, \mathbf{C}_V\}$ , the optimization objective  $\mathcal{L}$  is the cross-entropy between the ground truth occupancy value  $t \in [1, 255]$  and the corresponding predicted probability of each voxel  $\tilde{p}_t(x_i | \mathbf{C}_i; \mathbf{w})$ . This can be defined as follows:

$$\mathcal{L} = - \sum_i^V \log \tilde{p}_t(x_i | \mathbf{C}_i; \mathbf{w}). \quad (3)$$

## 4 Methodology

We propose a model-agnostic Spherical-Coordinate-based learned Point cloud compression (SCP) method, which efficiently leverages the features of LiDAR PCs. Furthermore, we introduce a multi-level Octree method to solve the higher reconstruction errors problem for distant voxels in the Spherical-coordinate-based Octree.

### 4.1 Spherical-Coordinate-based Learned Point Cloud Compression

The circular shapes and azimuthal angle invariance features in LiDAR PCs lead to a high degree of redundancy. In common-used Cartesian coordinates, redundant points are segmented into discrete voxels, as shown in Fig. 1(a). This

segmentation creates an unstable context, in which nearby voxels may not be relevant.

To leverage both features of LiDAR PCs, we propose the Spherical-Coordinate-based learned Point cloud Compression (SCP) method, which converts the points from Cartesian coordinates to Spherical coordinates. When looking up-down, the Spherical-coordinate-based Octree has the same structure as the Cylindrical one, as shown in Fig. 1(a)-left. Points in the same chain are assigned together, making better usage of circular shapes. On the other hand, when looking horizontally from the original point, the Spherical-coordinate-based Octree (Fig. 1(c)) is more likely to assign the points in the same chain to the same voxel compared with the Cylindrical one (Fig. 1(a)-right), harnessing the azimuthal angle invariance feature. Furthermore, the representation of circular structures in Spherical coordinates is simplified from quadratic to linear, making the prediction problem easier to solve, as illustrated in Fig. 3.

When constructing Octree in Spherical coordinates, the quantization procedure differs from that in Cartesian coordinates. The variation range for the  $\rho$ ,  $\theta$  and  $\varphi$  coordinates in Spherical coordinates are  $[0, \rho_{max}]$ ,  $[0, 2\pi)$  and  $[0, \pi]$ , respectively. The  $\rho_{max}$  varies in different point clouds. When quantizing the point clouds, we adopt the quantization step  $q$  of EHEM (Song et al. 2023) to the  $\rho$  coordinate, noted as  $q_\rho = q$ . Therefore, the total number of bins for  $\rho$  coordinate is  $b = \lceil \rho_{max}/q_\rho \rceil$ . Subsequently, we divide the ranges of the  $\theta$  and  $\varphi$  coordinates by  $b$  separately to generate their respective quantization steps, as demonstrated in Eq.(4).

$$\begin{aligned} q_\theta &= 2\pi/(b-1) \approx \frac{2\pi q}{\rho_{max}}, \\ q_\varphi &= \pi/(b-1) \approx \frac{\pi q}{\rho_{max}}, \end{aligned} \quad (4)$$

where  $q$  is the quantization step. By setting these  $q_\theta$  and  $q_\varphi$ , the bin number of each coordinate are the same.

## 4.2 Multi-Level Octree for SCP

In the Spherical-coordinate-based Octree, the distance  $\rho$  is positively related to the reconstruction error, causing the higher reconstruction error of distant voxels. To maintain a reconstruction error lower or similar to that in Cartesian coordinates, we propose a multi-level Octree for SCP, which allocates additional levels to distant voxels. We initially discuss the relation between distant voxels and reconstruction errors of the quantized point cloud in Cartesian and Spherical coordinates, then illustrate our multi-level Octree method.

For Cartesian coordinates, the upper bound of the error can be expressed as follows:

$$\varepsilon_c = \max_i \|p_i - \hat{p}_i\|_2 \leq \frac{\sqrt{3}q}{2}, \quad (5)$$

where  $p_i$  represents the original position of point  $i$ , and  $\hat{p}_i$  is its position after quantization,  $q$  is the quantization step size.

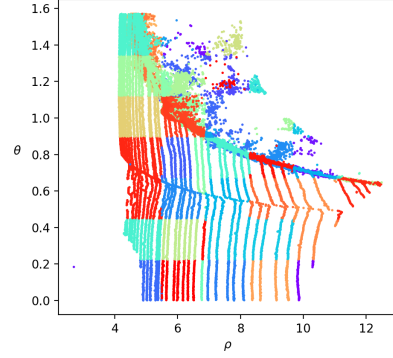


Figure 3: The projections of point positions in Spherical coordinates onto the  $\rho\theta$ -plane. The left parts, which represent circular shapes in the point cloud, are nearly straight lines, which is simpler for the compression of points.

It is obvious that this error is uniformly distributed throughout the entire space of Cartesian coordinates because the upper bound is only related to the quantization step. The complete derivation can be found in Appendix.1.

In the Spherical coordinate system, however, the voxels' reconstruction error is non-uniform. As depicted in Fig. 2, the further a voxel (with a larger  $\rho$  value) is from the origin, the larger its size. This characteristic leads to a higher upper bound of reconstruction error for distant voxels. As shown in Eq.(6), the reconstruction error  $\varepsilon_s$  linearly correlated with the value of the  $\rho$  coordinate.

$$\varepsilon_s = \max_i \|p_i - \hat{p}_i\|_2 \leq \frac{\sqrt{5}\pi q}{2\rho_{max}} \rho. \quad (6)$$

We put the proof into the Appendix.1 and further discuss the quantization results in Sec. 5.2.

Based on the above findings, if we allocate additional levels (depths) to the distant areas in the Octree, each added level will reduce the quantization step size of the distant area from  $q$  to  $\frac{1}{2}q$ , which in turn halves  $\varepsilon_s$  according to Eq.(6). Motivated by this, we propose a multi-level Octree method to reduce the reconstruction error of distant voxels by adding additional levels. Specifically, we divide the point cloud into  $N$  parts to assign different numbers of additional levels. Each part has  $n \in \{0, 1, \dots, N-1\}$  additional levels with  $\rho_n \in [t_n \rho_{max}, t_{n+1} \rho_{max})$ , where  $0 \leq t_n < t_{n+1} < 1$ ,  $t_0 = 0$ ,  $t_N = 1$ . The assigned extra levels can be represented by the reduction of the quantization  $q_n = \frac{q}{2^n}$ , making the reconstruction error upper bound of each part  $n$  lower or similar to the upper bound of  $\varepsilon_c$ , which can be expressed as

$$\varepsilon_n \leq \frac{\sqrt{5}\pi q_n}{2\rho_{max}} \cdot \frac{t_n + t_{n+1}}{2} \rho_{max} = \frac{\sqrt{5}\pi q(t_n + t_{n+1})}{2^{n+2}}, \quad (7)$$

where we assign  $n$  additional levels for the part  $n$ . In our experiments, we describe how to pick the optimal  $t_n$  for each part to keep  $\varepsilon_n \leq \varepsilon_c$ .



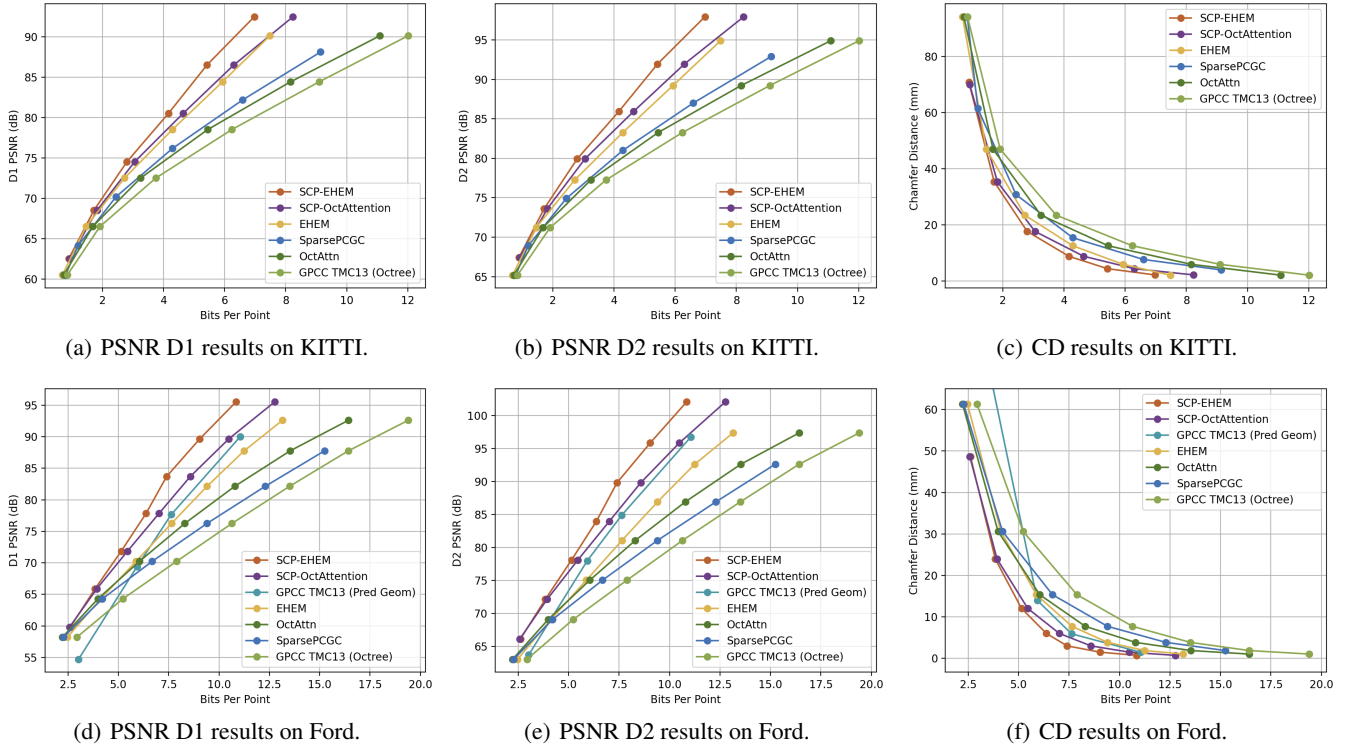


Figure 4: Quantitative rate-distortion results of our SCP-EHEM and SCP-OctAttn models on KITTI (top) and Ford (bottom) datasets. The baselines are EHEM (Song et al. 2023), SparsePCGC (Wang et al. 2022), OctAttention (Fu et al. 2022) and G-PCC TMC13 (ISO/IEC JTC 1/SC 29/WC 7 2021) with either Octree or predictive geometry. Predictive geometry is only available for the Ford dataset, as the KITTI dataset lacks the necessary sensor information for the calculation of predictive geometry.

## 5 Experiments

### 5.1 Experiment Settings

**Datasets** We compare all the baseline models and SCP on two LiDAR PC datasets, SemanticKITTI (Behley et al. 2019) and Ford (Pandey, McBride, and Eustice 2011). SemanticKITTI, abbreviated as KITTI, comprises 43,552 LiDAR scans obtained from 22 point cloud sequences. The default split for training includes sequences 00 to 10, while sequences 11 to 21 are used for evaluation. We quantize them with a quantization step of  $\frac{400}{2^D-1}$  with Octree depth  $D$ , the same as EHEM (Song et al. 2023). The Ford dataset, utilized in the MPEG point cloud compression standardization, includes three sequences, each containing 1,500 scans. We adhere to the partitioning of the MPEG standardization, where sequence 01 is used for training and sequences 02 and 03 for evaluation. Each sequence in the Ford dataset contains an average of 100,000 points per frame and is quantized to a precision of 1mm. We set the quantization step for it to  $2^{18-D}$  with Octree depth  $D$ , also the same as EHEM.

**Metrics** We evaluate point cloud compression methods across two dimensions: rate and distortion. The rate is measured in bits per point (bpp), which is the quotient of the bitstream length and the number of points. For distortion, we employ the most frequently used three metrics: point-to-point PSNR (D1 PSNR), point-to-plane PSNR (D2 PSNR) (ISO/IEC JTC 1/SC 29/WG 7 2021), and Cham-

fer distance (CD). These metrics are adopted in the former methods, such as EHEM (Song et al. 2023) and OctAttention (Fu et al. 2022), so it is efficient to compare SCP with the former methods on these metrics. We also employ BD-Rate (Bruylants, Munteanu, and Schelkens 2015) to illustrate our experimental results clearly. Following EHEM (Song et al. 2023) and (Biswas et al. 2020), we set the peak value of PSNR to 59.70 for KITTI and 30000 for Ford.

**Implementation Details** Our experiments are conducted on OctAttention (Fu et al. 2022) and our reproduced EHEM (Song et al. 2023), as the official implementation of EHEM is not provided. During training, we input the information of Spherical-coordinate-based Octree to the models, including the following information: (1) Octant: the integer order of the current voxel in the parent voxel, in the range of  $[1, 8]$ ; (2) Level: the integer depth of the current voxel in the Octree, in the range of  $[1, 16]$  and  $[1, 17]$  for KITTI and Ford, respectively; (3) Occupancy, Octant, Level of ancient voxels: All the information of former levels. We trace back 3 levels, the same as OctAttention (Fu et al. 2022); (4) Position: three floating-point positions of the current voxel in the Spherical coordinates, regularized to range  $[0, 1]$ .

For the multi-level Octree method, we can deduce from Eq.(5) and Eq.(6) that  $\varepsilon_s = \varepsilon_c, 2\varepsilon_c, 4\varepsilon_c$  at approximately  $\rho = 0.247\rho_{max}, 0.493\rho_{max}, 0.986\rho_{max}$ , respectively. On the other hand, SCP predicts the distribution of each part

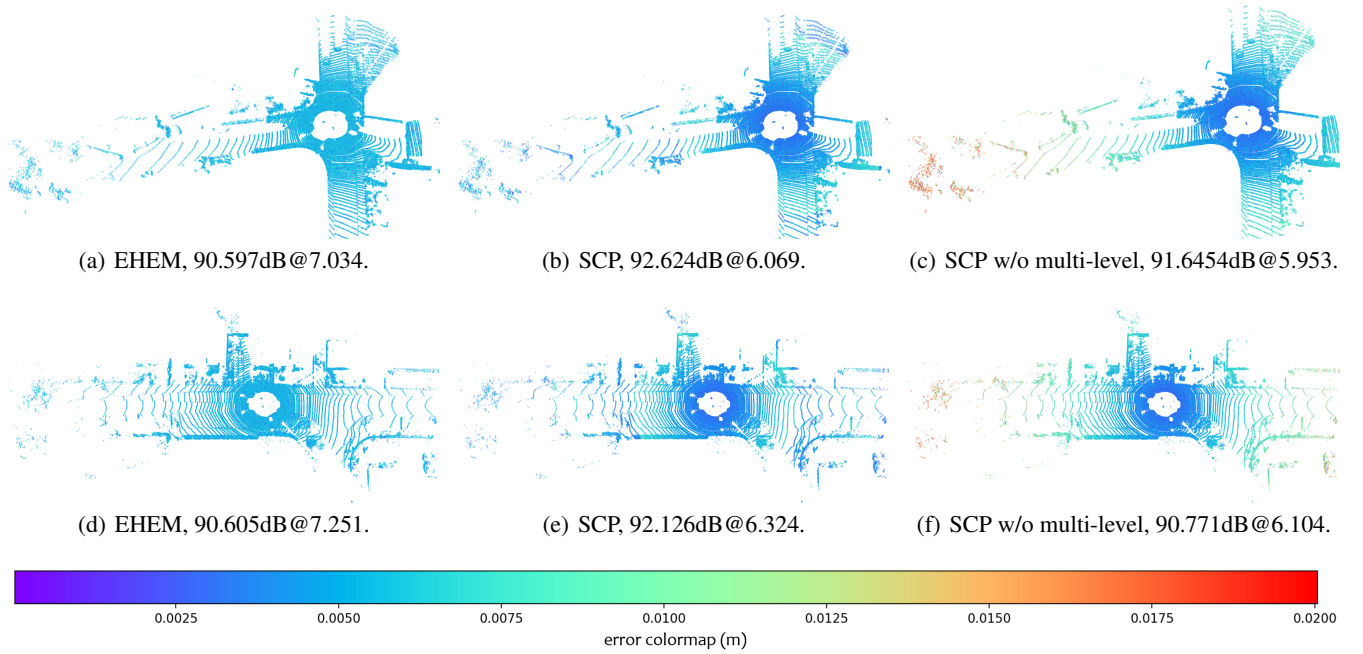


Figure 5: The figures compare the reconstruction errors on point clouds No. 000000 in Sequence 11 (a, b, c) and No. 000000 in Sequence 16 (d, e, f) from KITTI (Behley et al. 2019), among the baseline EHEM (Song et al. 2023) method in (a, d), our SCP-EHEM method in (b, e), and the SCP-EHEM without a multi-level Octree in (c, f). The metrics are D1 PSNR @ bpp. The error colormap is displayed below the figures, where purple indicates the lowest error, and red represents the highest error. It is evident that the central parts of the point clouds in (b, e) have significantly lower reconstruction errors than the baseline method shown in (a, d). Conversely, the distant parts in (c, f) have much higher reconstruction errors than the central parts, but this is mitigated by implementing the multi-level Octree as depicted in (b, e).

separately, which means we repeat the processing of the first several levels  $N$  times. Hence, for efficiency,  $t_n$  is set to the inverse of the power of 2, which utmost reduces repetition. In our experiments, to keep the reconstruction error of SCP lower than that in Cartesian coordinates, we set  $N = 3$  and  $t_n \in \{0, \frac{1}{4}, \frac{1}{2}\}$ , which divides the point clouds into 3 parts: the inner part with  $\rho \in [0, \frac{1}{4}\rho_{max})$ , the middle part with  $\rho \in [\frac{1}{4}\rho_{max}, \frac{1}{2}\rho_{max})$ , and outer part with  $\rho \in [\frac{1}{2}\rho_{max}, \rho_{max}]$ . This splitting method constrains the upper bound of the reconstruction error to be lower or equal to the one in Cartesian coordinates for most areas, thereby achieving similar or better reconstruction results for both distant and central parts in LiDAR PCs.

We train the EHEM and OctAttention models on KITTI and Ford datasets for 20 and 150 epochs, respectively. For all experiments, we employ the default Adam optimizer (Kingma and Ba 2014) with a learning rate of  $10^{-4}$ . All the experiments are done on the server with 8 NVIDIA A100 GPUs and 2 AMD EPYC 7742 64-Core CPUs.

**Baselines** We use recent methods as our baseline to verify the effectiveness of our SCP method. These methods include the state-of-the-art EHEM (Song et al. 2023), which employs the Swin Transformer (Liu et al. 2021) and checkerboard (He et al. 2021a) to compress point clouds; the sparse-CNN-based method SparsePCGC (Wang et al. 2022), which achieves high compression performance with an end-to-end

Method	Depth=12	Depth=14	Depth=16
G-PCC	0.22 / 0.06	0.63 / 0.21	1.05 / 0.39
EHEM	0.60 / 0.57	1.48 / 1.57	2.92 / 3.13
SCP-E w/o	0.63 / 0.62	1.73 / 1.86	3.21 / 3.49
SCP-EHEM	1.16 / 1.11	2.34 / 2.41	3.92 / 4.09

Table 1: Encoding/decoding times (in seconds) for a D-depth octree on KITTI dataset among GPCC (ISO/IEC JTC 1/SC 29/WC 7 2021), EHEM (Song et al. 2023), SCP-EHEM without multi-level Octree (SCP-E w/o), and SCP-EHEM. Runtimes for G-PCC are total times.

scheme; the aforementioned OctAttention (Fu et al. 2022), which uses the Transformer and sibling voxel contexts; and the MPEG G-PCC TMC13 (ISO/IEC JTC 1/SC 29/WC 7 2021) with either Octree or predictive geometry, which is the mainstream hand-crafted compression method. Note that the predictive geometry is only available for the Ford dataset since the KITTI dataset lacks the necessary sensor information for the calculation of predictive geometry.

## 5.2 Experimental Results

We designate SCP with a multi-level Octree as the default method, referred to as “SCP”, while the SCP method without a multi-level Octree is labeled as “SCP w/o multi-level” or “SCP w/o”. The SCP methods with EHEM (Song et al. 2023) and OctAttention (Fu et al. 2022) as the backbone are

represented as “SCP-EHEM” and “SCP-OctAttn”, respectively.

**Quantitative results** As depicted in Fig. 4, our SCP-EHEM models achieve significant improvement when compared with all the baselines. SCP achieves a 61.23% D1 PSNR BD-Rate gain on the KITTI dataset and 72.54% on the Ford dataset when compared with Octree-based G-PCC. On the other hand, SCP-EHEM and SCP-OctAttention models outperform the baseline methods by 13.02% and 29.14% D1 PSNR BD-rate improvement on the KITTI dataset, respectively; 25.54% and 24.78% on the Ford dataset, respectively. Remarkably, SCP-OctAttention even surpasses the original EHEM method, which has an 8 times larger receptive field than OctAttention. Our results on D2 PSNR and CD metrics also significantly outperform the previous method, demonstrating the robustness of SCP in efficiently compressing various point clouds under different driving environments for point cloud acquisition. For the results of predictive-geometry-based G-PCC on the Ford dataset, it has a much better performance than the Octree-based one except for the lowest reconstruction quality. However, it is surpassed by both SCP-EHEM and SCP-OctAttention because of the lack of context information. All these experiments showcase the universality of our SCP, which can be applied to various learned methods to fully leverage the circular feature of LiDAR PCs and improve the performance of these methods.

We show the inference time comparisons among G-PCC, the reproduced EHEM, SCP-EHEM without multi-level Octree (SCP-E w/o), and SCP-EHEM in Table 1. The reconstruction performance of SCP-E w/o is better than the original Cartesian-coordinate-based EHEM because Spherical-coordinate-based Octree has lower reconstruction error in the central parts, which contain most points in the point cloud. This reserves more individual points after quantization, leading to a correspondingly longer processing time. On the other hand, one limitation of SCP-EHEM is that it repeats calculations of the beginning levels for each part, resulting in time overhead, which can be eliminated by processing the former levels together for all 3 parts. We will solve the problem of this overhead in our future work.

**Qualitative results** As depicted in Fig. 5, we visualize the reconstruction errors for point clouds in the KITTI dataset. The errors are represented with a rainbow color scheme, where purple indicates lower error and red signifies higher error. It is evident that the central parts of Fig. 5(b) and Fig. 5(e) have lower errors than those of Fig. 5(a) and Fig. 5(d), while the distant parts of our method exhibit similar reconstruction errors. In another perspective, the distant area of Fig. 5(c) and Fig. 5(f) exhibit significantly higher errors compared to the central areas. This issue is substantially mitigated following the application of our multi-level Octree method, as demonstrated in Fig. 5(b) and Fig. 5(e).

### 5.3 Ablation Study

In order to validate the effectiveness of SCP and the multi-level Octree method, we conducted ablation studies on them, as illustrated in Fig. 6. For the selection of metric, we find the curve tendencies of 3 metrics in Fig. 4 are similar, so we

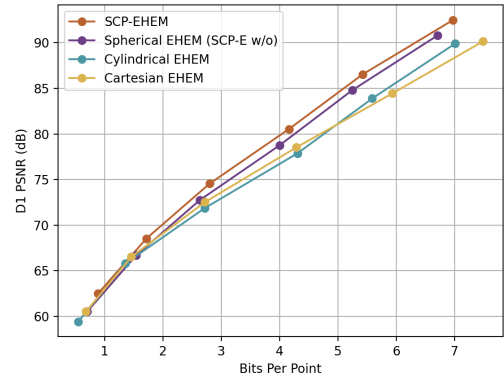


Figure 6: The ablation experiments among our SCP-EHEM, the Spherical-coordinate-based EHEM (SCP-EHEM without multi-level Octree method), the Cylindrical-coordinate-based EHEM, and the Cartesian-coordinate-based EHEM (original EHEM). The BD-Rate gain between SCP-EHEM to the rest three methods are 5.98%, 14.61%, and 13.02%, respectively.

follow the ablation settings of EHEM, using D1 PSNR as the metric.

To verify the good performance of SCP, we experiment on all three coordinate systems: Spherical, Cylindrical, and Cartesian, with EHEM as the backbone model. Note that the Cartesian-coordinate-based EHEM is the original EHEM. These experiments are conducted without the multi-level Octree method because it is designed for angle-based coordinate systems and is not applicable to Cartesian-coordinate-based Octree. As shown in Fig. 6, Spherical-coordinate-based EHEM (Spherical EHEM) is better than both the Cartesian-coordinate-based one (Cartesian EHEM) and the Cylindrical-coordinate-based one (Cylindrical EHEM), achieving BD-Rate improvements at 7.05% and 5.87%, respectively. On the other hand, for the ablation study on the multi-level Octree method, our SCP-EHEM model outperforms the version without our multi-level Octree method (SCP-E w/o) with a 5.98% D1 PSNR BD-Rate gain, proving the effectiveness of our method.

## 6 Conclusion

We introduce a model-agnostic Spherical-Coordinate-based learned Point cloud compression (SCP) method that effectively leverages the circular shapes and azimuthal angle invariance feature present in spinning LiDAR point clouds. Concurrently, we address the higher reconstruction error issue in distant areas of the Spherical-coordinate-based Octree by implementing a multi-level Octree method. Our techniques exhibit high universality, making them applicable to a wide range of learned point cloud compression methods. Experimental results on two backbone methods, EHEM and OctAttention, exhibit the high effectiveness of our SCP and multi-level Octree method. On the other hand, our methods still have the potential to be improved on the inference time, which will be done in our future work.

## References

- Behley, J.; Garbade, M.; Milioto, A.; Quenzel, J.; Behnke, S.; Stachniss, C.; and Gall, J. 2019. Semantickitti: A dataset for semantic scene understanding of lidar sequences. In *Proceedings of the IEEE/CVF international conference on computer vision*, 9297–9307.
- Biswas, S.; Liu, J.; Wong, K.; Wang, S.; and Urtasun, R. 2020. Muscle: Multi sweep compression of lidar using deep entropy models. *Advances in Neural Information Processing Systems*, 33: 22170–22181.
- Bruylants, T.; Munteanu, A.; and Schelkens, P. 2015. Wavelet based volumetric medical image compression. *Signal processing: Image communication*, 31: 112–133.
- Chen, Z.; Qian, Z.; Wang, S.; and Chen, Q. 2022. Point Cloud Compression with Sibling Context and Surface Priors. In *European Conference on Computer Vision*, 744–759. Springer.
- Choe, J.; Joung, B.; Rameau, F.; Park, J.; and Kweon, I. S. 2021. Deep point cloud reconstruction. *arXiv preprint arXiv:2111.11704*.
- Cui, M.; Long, J.; Feng, M.; Li, B.; and Kai, H. 2023. OctFormer: Efficient Octree-Based Transformer for Point Cloud Compression with Local Enhancement. In *Proceedings of the AAAI Conference on Artificial Intelligence*, volume 37, 470–478.
- Fernandes, D.; Silva, A.; Névoa, R.; Simões, C.; Gonzalez, D.; Guevara, M.; Novais, P.; Monteiro, J.; and Melo-Pinto, P. 2021. Point-cloud based 3D object detection and classification methods for self-driving applications: A survey and taxonomy. *Information Fusion*, 68: 161–191.
- Fu, C.; Li, G.; Song, R.; Gao, W.; and Liu, S. 2022. Octattention: Octree-based large-scale contexts model for point cloud compression. In *Proceedings of the AAAI Conference on Artificial Intelligence*, volume 36, 625–633.
- Garcia, D. C.; and de Queiroz, R. L. 2018. Intra-frame context-based octree coding for point-cloud geometry. In *2018 25th IEEE International Conference on Image Processing (ICIP)*, 1807–1811. IEEE.
- He, D.; Zheng, Y.; Sun, B.; Wang, Y.; and Qin, H. 2021a. Checkerboard context model for efficient learned image compression. In *Proceedings of the IEEE/CVF Conference on Computer Vision and Pattern Recognition*, 14771–14780.
- He, Y.; Huang, H.; Fan, H.; Chen, Q.; and Sun, J. 2021b. Ffb6d: A full flow bidirectional fusion network for 6d pose estimation. In *Proceedings of the IEEE/CVF Conference on Computer Vision and Pattern Recognition*, 3003–3013.
- He, Y.; Sun, W.; Huang, H.; Liu, J.; Fan, H.; and Sun, J. 2020. Pvn3d: A deep point-wise 3d keypoints voting network for 6dof pose estimation. In *Proceedings of the IEEE/CVF conference on computer vision and pattern recognition*, 11632–11641.
- Huang, L.; Wang, S.; Wong, K.; Liu, J.; and Urtasun, R. 2020. Otsqueeze: Octree-structured entropy model for lidar compression. In *Proceedings of the IEEE/CVF conference on computer vision and pattern recognition*, 1313–1323.
- Huang, Y.; Peng, J.; Kuo, C.-C. J.; and Gopi, M. 2008. A generic scheme for progressive point cloud coding. *IEEE Transactions on Visualization and Computer Graphics*, 14(2): 440–453.
- ISO/IEC JTC 1/SC 29/WG 7. 2019. Predictive Geometry Coding. M51012.
- ISO/IEC JTC 1/SC 29/WG 7. 2021. Mpeg g-pcc tmc13. <https://github.com/MPEGGroup/mpeg-pcc-tmc13>.
- ISO/IEC JTC 1/SC 29/WG 7. 2021. Common test conditions for g-pcc. N00106.
- Jackins, C. L.; and Tanimoto, S. L. 1980. Oct-trees and their use in representing three-dimensional objects. *Computer Graphics and Image Processing*, 14(3): 249–270.
- Kammerl, J.; Blodow, N.; Rusu, R. B.; Gedikli, S.; Beetz, M.; and Steinbach, E. 2012. Real-time compression of point cloud streams. In *2012 IEEE international conference on robotics and automation*, 778–785. IEEE.
- Kingma, D. P.; and Ba, J. 2014. Adam: A method for stochastic optimization. *arXiv preprint arXiv:1412.6980*.
- Li, R.; Li, X.; Heng, P.-A.; and Fu, C.-W. 2021. Point cloud upsampling via disentangled refinement. In *Proceedings of the IEEE/CVF conference on computer vision and pattern recognition*, 344–353.
- Li, Y.; Ma, L.; Zhong, Z.; Liu, F.; Chapman, M. A.; Cao, D.; and Li, J. 2020. Deep learning for lidar point clouds in autonomous driving: A review. *IEEE Transactions on Neural Networks and Learning Systems*, 32(8): 3412–3432.
- Liu, Z.; Lin, Y.; Cao, Y.; Hu, H.; Wei, Y.; Zhang, Z.; Lin, S.; and Guo, B. 2021. Swin transformer: Hierarchical vision transformer using shifted windows. In *Proceedings of the IEEE/CVF international conference on computer vision*, 10012–10022.
- Nguyen, D. T.; Quach, M.; Valenzise, G.; and Duhamel, P. 2021a. Learning-based lossless compression of 3d point cloud geometry. In *ICASSP 2021-2021 IEEE International Conference on Acoustics, Speech and Signal Processing (ICASSP)*, 4220–4224. IEEE.
- Nguyen, D. T.; Quach, M.; Valenzise, G.; and Duhamel, P. 2021b. Learning-based lossless compression of 3d point cloud geometry. In *ICASSP 2021-2021 IEEE International Conference on Acoustics, Speech and Signal Processing (ICASSP)*, 4220–4224. IEEE.
- Pandey, G.; McBride, J. R.; and Eustice, R. M. 2011. Ford campus vision and lidar data set. *The International Journal of Robotics Research*, 30(13): 1543–1552.
- Quach, M.; Valenzise, G.; and Dufaux, F. 2019. Learning convolutional transforms for lossy point cloud geometry compression. In *2019 IEEE international conference on image processing (ICIP)*, 4320–4324. IEEE.
- Que, Z.; Lu, G.; and Xu, D. 2021. Voxelcontext-net: An octree based framework for point cloud compression. In *Proceedings of the IEEE/CVF Conference on Computer Vision and Pattern Recognition*, 6042–6051.
- Silva, A. L.; Oliveira, P.; Durães, D.; Fernandes, D.; Névoa, R.; Monteiro, J.; Melo-Pinto, P.; Machado, J.; and Novais, P. 2023. A Framework for Representing, Building and Reusing



Novel State-of-the-Art Three-Dimensional Object Detection Models in Point Clouds Targeting Self-Driving Applications. *Sensors*, 23(14): 6427.

Song, R.; Fu, C.; Liu, S.; and Li, G. 2023. Efficient Hierarchical Entropy Model for Learned Point Cloud Compression. In *Proceedings of the IEEE/CVF Conference on Computer Vision and Pattern Recognition (CVPR)*, 14368–14377.

Sridhara, S. N.; Pavez, E.; and Ortega, A. 2021. Cylindrical coordinates for LiDAR point cloud compression. In *2021 IEEE International Conference on Image Processing (ICIP)*, 3083–3087. IEEE.

Unno, K.; Matsuzaki, K.; Komorita, S.; and Kawamura, K. 2023. Rate-Distortion Optimized Variable-Node-size Trisoup for Point Cloud Coding. In *ICASSP 2023-2023 IEEE International Conference on Acoustics, Speech and Signal Processing (ICASSP)*, 1–5. IEEE.

Wang, C.; Xu, D.; Zhu, Y.; Martín-Martín, R.; Lu, C.; Fei-Fei, L.; and Savarese, S. 2019. Densefusion: 6d object pose estimation by iterative dense fusion. In *Proceedings of the IEEE/CVF conference on computer vision and pattern recognition*, 3343–3352.

Wang, J.; Ding, D.; Li, Z.; Feng, X.; Cao, C.; and Ma, Z. 2022. Sparse tensor-based multiscale representation for point cloud geometry compression. *IEEE Transactions on Pattern Analysis and Machine Intelligence*.

## 7 Appendix

### 7.1 Reconstruction error of Cartesian coordinates and Spherical coordinates

We illustrate the derivation of Eq.(5) and Eq.(6) in this section. We use the  $L2$ -norm to evaluate the reconstruction error. This  $L2$ -norm is used in all three metrics in our experiments.

For the Octree in Cartesian coordinates, the leaf voxels are cubes whose side length is quantization step  $q$ . The position of a voxel is the center of it, marked as  $(x_c, y_c, z_c)$ . The upper bound of reconstruction error can be reached at the corners of the cube, one of which can be written as  $(x_c + \frac{q}{2}, y_c + \frac{q}{2}, z_c + \frac{q}{2})$ . Therefore, the upper bound of reconstruction error in Cartesian coordinates is

$$\varepsilon_c \leq \sqrt{3(\frac{q}{2})^2} = \frac{\sqrt{3}q}{2}. \quad (8)$$

To compare with former methods, we need to convert Spherical coordinates back to Cartesian coordinates for reconstruction error calculation. In Spherical coordinates, the size of voxels is only relevant to coordinate  $\rho$ , therefore, we analyze the one voxel beside coordinate  $x$ , as the green box shown in Fig. 7, which is easier for derivation. The voxel center can be marked as  $(\rho_c \cos \frac{q_\theta}{2}, \rho_c \sin \frac{q_\theta}{2}, \rho_c \sin \frac{q_\theta}{4})$ . We use  $q_\theta$  to replace  $q_\varphi$  according to Eq.(4). In the most situation,  $q$  is much smaller than  $\rho_c$ , so we can set  $\cos \frac{q_\theta}{2} = 1$ ,  $\sin \frac{q_\theta}{2} = \sin \frac{q_\theta}{4} = 1$ . Then the position can be rewritten as:  $(\rho, \rho \frac{q_\theta}{2}, \rho \frac{q_\theta}{4})$ . On the other hand, one of the furthest points in the voxel is indicated in Fig. 7. The position of it is  $(\rho_c + \frac{q}{2}, 0, 0)$ , which can be approximated as  $(\rho_c, 0, 0)$  since  $q$  is much smaller than  $\rho_c$ . In conclusion, the upper bound of the reconstruction error can be derived by calculating the distance between these two points, as shown in Eq.(9).

$$\varepsilon_s \leq \sqrt{(\rho_c \frac{q_\theta}{2})^2 + (\rho_c \frac{q_\theta}{4})^2} = \frac{\sqrt{5}}{4} \rho_c q_\theta = \frac{\sqrt{5}\pi q}{2\rho_{max}} \rho_c. \quad (9)$$

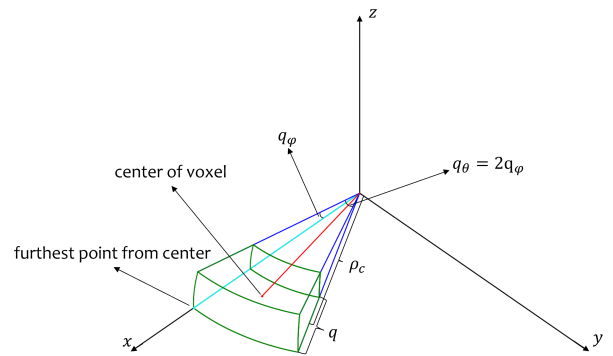


Figure 7: Derivation for Eq.(6).